The Effect of Tin Doping on α-Fe_2O_3 Photoanodes for Water Splitting*

Christopher D. Bohn[1†], Amit K. Agrawal[1,2], Erich C. Walter[1,3], Mark D. Vaudin[4], Andrew A. Herzing[5], Paul M. Haney[1], A. Alec Talin[1], Veronika A. Szalai[1†]

[1] Center for Nanoscale Science and Technology, National Institute of Standards and Technology, Gaithersburg, Maryland, 20899, USA.

[2] Dept. of Electrical Engineering and Computer Science, Syracuse University, Syracuse, NY, 13244, USA.

[3] Institute for Research in Electronics and Applied Physics (IREAP), University of Maryland, College Park, MD 20742, USA.

[4] Ceramics Division, National Institute of Standards and Technology, Gaithersburg, MD, 20899, USA.

[5] Surface and Microanalysis Science Division, National Institute of Standards and Technology, Gaithersburg, MD 20899, USA.

[†]Corresponding authors. Phone: 301-975-3792 (VAS), 301-975-4236 (CDB), Fax: 301-975-2303, Email: veronika.szalai@nist.gov, christopher.bohn@nist.gov

***** Certain commercial equipment, instruments, and materials are identified in this paper to foster understanding. Such identification does not imply recommendation or endorsement by the National Institute of Standards and Technology, nor does it imply that the materials or equipment identified are the best available for the purpose.

Abstract: (186 words)

Sputter-deposited films of α-Fe_2O_3 of thickness 600 nm were investigated as photoanodes for solar water splitting and found to have photocurrents as high as 0.8 mA/cm^2 at 1.23 V *vs.* the reversible hydrogen electrode (RHE). Sputter-deposited films, relative to nanostructured samples produced by hydrothermal synthesis,[1,2] permit facile characterization of the role and placement of dopants. The Sn dopant concentration in the α-Fe_2O_3 varies as a function of distance from the fluorine-doped tin oxide (FTO) interface and was quantified using secondary ion mass spectrometry (SIMS) to give a mole fraction of cations of approximately 0.02 % at the electrolyte interface. Additional techniques for determining dopant density including energy dispersive X-ray spectroscopy (EDS), electron energy loss spectroscopy (EELS), electrochemical impedance spectroscopy (EIS) and conductivity measurements are compared and discussed. Based on this multi-faceted data set, we conclude that not all dopants present in the α-Fe_2O_3 are active. Dopant activation, rather than just increasing surface area or dopant concentration, is critical for improving metal oxide performance in water splitting. A more complete understanding of dopant activation will lead to further improvements in the design and response of nanostructured photoanodes.

Keywords:

iron oxide, water splitting, photoanode, oxygen production, dopant activation

Introduction:

The sun delivers more than 120,000 TW of power to the Earth's surface, nearly 10,000 times the current global consumption rate of 15 TW.[3] The viability of solar radiation as a major energy source requires the development of efficient and affordable energy collection and storage solutions to meet stable supply requirements. One environmentally benign route to achieving this goal is to employ solar radiation to separate water into H_2 and O_2.

Hematite, α-Fe_2O_3, has shown potential as a photoanode for water splitting because it possesses several desirable properties including: a bandgap between 1.9 eV and 2.2 eV that maximizes absorption from the solar spectrum,[4] stability in an aqueous environment under typical operating conditions,[5] abundance in the earth's crust and affordability. Despite these advantages, hematite exhibits a low electrical mobility[6,7,8] (0.01 $cm^2 \cdot V^{-1} \cdot s^{-1}$ to 0.1 $cm^2 \cdot V^{-1} \cdot s^{-1}$), short hole diffusion length[9,10] (2 nm to 4 nm), and thermodynamically requires an applied overpotential to overcome energy band misalignment. Doping can mitigate some of these deficiencies, however, the measurement of dopant concentrations and interpretation of the role of dopants on material properties remains challenging. Recently, markedly enhanced photocurrents have been obtained by annealing thin layers of α-Fe_2O_3 on fluorine-doped tin oxide (FTO) coatings on soda lime glass at 800 °C.[1,2,11] This enhancement has been attributed to n-type doping of the α-Fe_2O_3 phase with Sn, consistent with work using other group IVA/B dopants.[12,13] Unfortunately, only modest improvements in photocurrent have been realized by iteratively varying the dopant type, quantity and/or synthesis method.[14] A quantitative understanding of dopant incorporation, whether dopants are active or inactive, and the changes in

crystallinity and composition which accompany thermal treatments used for activation are among the issues that must be understood to improve photoanodes for water splitting.

Although nanostructured hematite exhibits improved performance relative to bulk materials,[1,10,15] nanostructuring complicates analysis of dopant effects because of uneven material coverage on the substrate. As a result, test structures comprising thin films have been pursued.[16,17] In this study we use sputtered films of α-Fe_2O_3 and diffuse the Sn from the substrate. The sputtered films analyzed in this paper exhibit photocurrents of 1.3 mA/cm^2 at 1.6 V *vs.* RHE (reversible hydrogen electrode) under 100 mW/cm^2 illumination, which is a factor of ≈ 1.5 higher than previously reported for sputtered films[12] and ≈ 1/3 the highest current density reported to date for α-Fe_2O_3 nanostructures.[15] The incorporation of Sn also dramatically reduces the resistivity of the film. The sputtered films permit quantitative determination of the Sn concentration in the hematite as a function of distance from the FTO interface. The effects of annealing- *i.a.* increased Sn doping, conductivity, and crystallinity- are discussed and should provide insight into designing nanostructured materials with further improved performance.

Experimental Methods:

Sample Fabrication

Hematite films (thickness 600 nm ± 30 nm) were prepared by reactively sputtering α-Fe_2O_3 from a Fe (mass fraction >99.95 %) target under a mixture of O_2 (12 mL/min) and Ar (50 mL/min) onto soda lime float glass coated with FTO (<10 Ω × m^2 / m^2). A control sample was prepared by sputtering 600 nm of α-Fe_2O_3 onto 200 nm Au with a 20 nm Cr adhesion layer on the glass side of the substrates. Alternate hematite samples of 300 nm ± 30 nm thickness were prepared following the hydrothermal synthesis method of Vayssieres.[1,17] Although some refer to these

structures as nanowires,[1,17] we refer to them as hydrothermal samples because no cylindrical form was recognizable from electron micrographs collected post annealing.

Electron microscopy

Samples were imaged using a scanning electron microscope (SEM) and a scanning transmission electron microscope (STEM) to probe sample morphology and crystal structure. To determine elemental distributions within the specimens, further characterization was performed using energy dispersive X-ray spectroscopy (EDS) and electron energy-loss spectroscopy (EELS). Additional experimental details regarding synthesis, fabrication, and characterization methods are provided in the Supporting Information (SI).

Electrochemistry

All experiments use 0.3 mL of sodium hydroxide (mass fraction > 97 %) diluted in deionized water to 1 mol/L at pH 13.6 as electrolyte, a coiled Pt wire counter electrode, and a Ag/AgCl reference electrode in saturated KCl. The electrochemical cell has a 5 mm × 15 mm window to define the illuminated area. Electrical contact to the FTO is made using gallium-indium eutectic (total mass fraction of Ga plus In >99.99 %), copper tape and silver paint. Prior to incident photon to current efficiency (IPCE) and Mott-Schottky experiments, the electrolyte is purged with N_2 for 30 min. Potentials are reported *vs.* RHE, using the conversion $E_{RHE} = E_{Ag/AgCl} + 0.059pH + E^{\circ}_{Ag/AgCl}$ with $E^{\circ}_{Ag/AgCl}$ = 0.1976 V.[19]

The light source is a 300 W ozone free xenon lamp with an AM 1.5 global filter to give 100 mW/cm^2 power, as measured by a broadband thermal power meter (Thorlabs, S310C) and confirmed by a reference solar cell (VLSI, SRC-1000-RTD-QZ). The scan rate is 10 mV/s for photocurrent measurements. For IPCE measurements, a monochromator delivers unchopped

light (beam diameter ≈ 3 mm) of 300 nm ≤ λ ≤ 800 nm in 10 nm increments with a bandwidth of 4 nm. The power at each wavelength is determined using a NIST traceable detector (Newport 70316NS); *e.g.*, the power at 500 nm is ≈ 100 μW. Transmission (93 %) through the quartz window was accounted for; loss through 4 mm of electrolyte is negligible. Mott-Schottky analysis is performed at 10^2 Hz, 10^3 Hz and 10^4 Hz in the dark using a root mean squared AC voltage of 25 mV. Linear and cylindrical fits are applied to determine the donor density, N_d, and flatband potential, V_{FB}.

Conductivity

To obtain the current-voltage characteristics, Au dots of area 0.16 mm^2 with a thickness of 200 nm are evaporated by electron beam deposition at a 45° angle on to the surface of samples which had previously been tested for photocurrent. The FTO is contacted to ground using gallium-indium eutectic, copper tape and one tungsten microprobe; the second probe is used to apply voltage to the Au contact. All measurements are made at room temperature and pressure and at a relative humidity of 33 %.

Secondary Ion Mass Spectrometry

Secondary ion mass spectrometry is performed by Charles Evans (Santa Clara, California). Six samples consisting of 600 nm of sputtered α-Fe_2O_3 are annealed at 500 °C for 2 h, and three of these are further annealed at 800 °C for 10 min prior to analysis. Details of the experimental conditions, area analyzed and instrument detection limit are in the SI. Sn in ZnO, a model oxide, is used for calibration; therefore, the reported concentration of Sn is approximate.

Results:

Photoelectrochemical performance

Figure 1(a) shows the photocurrent density, *J*, based on the geometric area versus applied potential for sputtered and hydrothermal α-Fe_2O_3 samples annealed in air at 500 °C for 2 h or at 500 °C for 2 h followed by 800 °C for 10 min. Importantly, we include dispersion bars calculated as one standard deviation of at least three independent measurements, which are shown as shading overlaid on the curves. The primary source of error was the temperature of the muffle furnace, which dropped by ≈20 °C upon introduction of the samples. For all samples annealed only at 500 °C, the potential sweeps in the light and dark are indistinguishable, as shown by the grey region in Fig. 1(a). After annealing at 800 °C, no dark current is observed below V_{RHE} = 1.6 V. Upon illumination, however, a photocurrent of 2.1 mA/cm^2 at 1.6 V is observed for the hydrothermal samples, which agrees well with data on similarly prepared material.[1,2] The onset of photocurrent at V_{RHE} = 0.8 V for the sputtered samples is 0.04 V lower than for the hydrothermal samples. For the control sample (600 nm of sputtered α-Fe_2O_3 on Au) that had undergone the same annealing treatments, the current under illumination is identical to the dark current (Figure S1 in SI), thus demonstrating that incorporation of Sn from the substrate is critical. The hydrothermal samples are remarkably reproducible, despite their non-uniform coverage (Figures S2 and S3 in SI). For sputtered films, 1.3 mA/cm^2 at 1.6 V is observed, which exceeds the highest previously reported value of *J* for sputtered films of 0.86 mA/cm^2.[12]

The incident photon to current efficiency (IPCE) at V_{RHE} = 1.23 V is shown in Figure 1(b) for samples annealed at 800 °C. The sputtered and hydrothermal samples show a peak IPCE efficiency of 10.1 % and 14.5 % at 340 nm, respectively. Converting these values to photocurrent density by integrating the product of IPCE (%) and the solar spectral irradiance at AM 1.5 global tilt ($W \cdot m^{-2} \cdot nm^{-1}$) with respect to wavelength λ (nm) and dividing by a conversion factor of 1240 eV·nm, gives 0.74 mA/cm^2 for sputtered films and 1.16 mA/cm^2 for

hydrothermal samples; the measured values from Fig. 1(a) were 0.82 mA/cm^2 and 1.17 mA/cm^2, respectively. This fidelity demonstrates that the experimental light source reproduces the AM 1.5G spectrum satisfactorily. The maximum solar to chemical conversion efficiencies are 0.081 % for the sputtered samples and 0.088 % for the hydrothermal samples at 1.05 V. These values are calculated using $\eta = (1.23 - V_{\mathrm{RHE}}) \times J/(100\ \mathrm{mW/cm^2})$, where V_{RHE} is the applied voltage in V, J is the measured photocurrent in mA/cm^2 and the denominator of 100 mW/cm^2 corresponds to the total incident power of irradiation.

Electron microscopy

SEM/EDS and STEM/EELS analyses are used to characterize the microstructure and composition of the sputtered α-Fe_2O_3 films. The hydrothermal samples are not analyzed because of the uneven coverage of the films on the FTO substrate (*i.e.* after synthesis FTO substrate is still exposed, Fig. S2(b)). Cross-sections of sputtered samples, of 100 nm ± 20 nm thickness are prepared using a focused ion beam (FIB) instrument as outlined in the SI. Figure 2 shows cross-sections of the α-Fe_2O_3 sputtered samples annealed at 500 °C for 2 h (a), followed by 800 °C for 10 min (b) prior to sectioning. By limiting the lamella thickness to 100 nm, spatial resolution with SEM and EDS is approximately a factor of five higher than the ≈ 0.5 µm diameter X-ray generation volume predicted from Monte Carlo simulations for a 10 kV electron beam impinging on bulk α-Fe_2O_3 (see details in SI).[20] EDS spectra are collected across each interface at the positions indicated by the black vertical lines in Figs. 2(a) and (b). X-ray intensity traces are shown in Fig. 2(c) for Fe $K_{\alpha 1}$ at 6.399 keV and Sn $L_{\alpha 1}$ at 3.444 keV. To account for small differences in sample thickness, raw X-ray counts for the sample annealed at 800 °C are scaled based on the integral number of Sn counts between -800 nm and 800 nm. No noticeable change in the diffusion gradient of Sn into α-Fe_2O_3 is observed between the two samples (Fig. 2(c)).

Taking the mean X-ray counts for Sn between -400 nm and -200 nm, dividing by the corresponding mean between 200 nm and 400 nm, and multiplying by the approximate percentage of Sn in SnO_2 (mole fraction of 33.3 %) gives estimates for the mole fraction of Sn of 1.0 % for both samples, independent of scaling. This value is an approximation, since a standards-based analysis was not pursued, but our results demonstrate that the approximate Sn doping level is considerably lower than the cation mole fraction of 10 % previously reported for samples prepared using an almost identical method.[1]

To further characterize the structural morphology and to attempt to quantify the low Sn concentrations, STEM high-angle annular dark-field (HAADF) imaging and EELS analyses are conducted. Due to the forward-bias of inelastic electron scattering in STEM, EELS has a minimal detectable mass up to three orders of magnitude lower than EDS for some elements.[21,22] A marked difference in grain crystallinity is immediately observable in STEM-HAADF images of sputtered samples annealed at 500 °C and 800 °C (Fig. 3(a) and (b)). The grains in the branched structure of the α-Fe_2O_3 at 500 °C (Fig 3(a)) are smoother after annealing (Fig 3(b)). There is also a decrease in contrast between the FTO and α-Fe_2O_3 layers after annealing at 800 °C, which could be attributable to densification.

Figs. 3(c) and (d) show EELS spectra for the sputtered α-Fe_2O_3 annealed at 500 °C and 800 °C, respectively. Both samples show abrupt O K-edge features at 532 eV, 542 eV and 563 eV that agree with published values for α-Fe_2O_3.[23] Also consistent with previous measurements on hematite, Fig. 3(d) shows abrupt Fe L_3 and L_2-edges corresponding to spin-orbit split levels $2p_{3/2}$ and $2p_{1/2}$, which are absent in the FTO layer, as expected. Following the analysis given in van Aken and Liebscher,[24] ratios of the integrated intensities of the L_3-edge and L_2-edge were

5.0 for the 500 °C and 6.0 for the 800 °C α-Fe_2O_3 samples, in good agreement with reported ratios (4.7 to 6.5) for Fe^{3+} in α-Fe_2O_3 .[23]

Incorporation of Sn is also analyzed by EELS. No detectable signals from the delayed $M_{4,5}$ edges of Sn at 493 eV and 485 eV are observed prior to the 532 eV O K-edge in Fig. 3(c) for both samples. The more positive background slope above 600 eV for the sample annealed at 800 °C could be possible evidence of the broad Sn $M_{4,5}$-edge, but variations in sample density with respect to the detector prevent firm conclusions.[24,25] Thus, the EELS results suggest that little Sn is present.

Mott-Schottky characterization

The Mott-Schottky technique is a method commonly used to determine the active concentration of dopants by measuring the capacitance of the space charge region formed at the semiconductor/electrolyte interface. The differential capacitance of the space charge layer as a function of applied potential for a planar n-type semiconductor electrode in contact with the electrolyte is given by the Mott-Schottky equation:[26]

$$\frac{1}{C^2} = \frac{2}{(q\epsilon\epsilon_0 N_d)}\left(V - V_{FB} - \frac{kT}{e}\right), \quad (1)$$

where C is the capacitance per unit area, q is the elementary charge, $\epsilon = 100$ is the dielectric constant assumed for the α-Fe_2O_3 semiconductor,[27,28] ϵ_0 is the permittivity of vacuum, N_d is the donor density, V is the applied DC voltage, V_{FB} is the flatband potential, k is Boltzmann's constant and T is the temperature. Equation (1) was derived using the one-dimensional Poisson equation and holds if:[29] (i) the semiconductor and electrolyte resistances are in series with the

space charge layer capacitance, (ii) no surface states exist, (iii) the distribution of donors is uniform and (iv) the interface is perfectly planar. The Sn donor density is then calculated as,[30]

$$N_d = 2/(e\epsilon\epsilon_0)[d(1/C^2)/dV]^{-1}, \quad (2)$$

Figure 4 shows a plot of Eq.1 for samples annealed at 500 °C for 2 h followed by 800 °C for 10 min (a, c) as well as for samples annealed at 500 °C for 2 h (b, d) at three frequencies: 10^2 Hz, 10^3 Hz and 10^4 Hz. Higher and lower frequencies are not used because at 10^5 Hz, a low capacitance is measured giving C^{-2} of $O(10^{14}\ \mathrm{cm^4/F^2})$ and at 10 Hz, the Lissajous plot of current versus voltage is not oval. The slopes in the C^{-2} *vs.* V plots decrease after annealing at 800 °C for both sputtered films and hydrothermal samples, indicating that the donor density increases with heating. This observation is consistent with increased incorporation of Sn atoms into the α-Fe_2O_3 lattice.

As observed previously for doped hematite,[2,14] our Mott-Schottky plots of the 800 °C annealed samples display parabolic behavior over 0.3 V to 0.9 V. This curvature may be explained by considering the electrostatics associated with the space-charge formation in the cylindrical grain geometry of the sputtered films[31] observed in Figs. 1-3 with radii of $R \approx 100$ nm. Solving the Poisson equation (see SI for calculation details), the capacitance for a cylindrical geometry is given by,

$$\frac{1}{C^2} = \left[\frac{R(R^2 - r^2)}{2\epsilon\epsilon_0 r_0^2}\right]^2. \quad (3)$$

Figure 4(e) shows the result using the linear fit from Eq.(1) over the range 0.6 V to 1.2 V. For comparison, Fig. 4(f) shows the Mott-Schottky data for the sputtered samples annealed at 800°C and fit with Eq.(3) after correcting for geometrical area (see SI for details) over the nonlinear

regime from 0.3 V to 0.9 V. The fitted N_d values vary by more than two orders of magnitude between the two cases (Table 1). Similar fitting is not pursued with the hydrothermal samples or the sputtered samples annealed at 500 °C as the former do not have clear cylindrical geometries and the latter do not display concavity in the C^{-2} *vs.* V plots at low applied voltage.

We conclude on the basis of results in Fig. 4 that $V_{FB} = 0.50 \pm 0.04$V from application of the linear model for the sputtered and hydrothermal samples at 800 °C, but that N_d cannot be determined with certainty. This conclusion is consistent with previous investigations of α-Fe_2O_3.[32] Specifically, the value of V_{FB} is close to that previously reported for Sn-doped hydrothermal samples of 0.49 V[1] and 0.4 V.[2] Inspection of the real impedance at 10^4 kHz obtained from the results in Figs. 4(a)-(d) gives values of 6 Ω and 10 Ω for 500 °C and 800 °C, respectively, for both the sputtered and hydrothermal samples. These impedance values are consistent with the FTO resistance (Table S1), rather than the resistance of the α-Fe_2O_3. Thus, assumption (i) regarding series resistances is incorrect as the gaps observed in the α-Fe_2O_3 layer in Figs. 1 and 2 extend to the substrate.

Conductivity

Because N_d is related to the specific resistance by $\rho = 1/(q\mu N_d)$, where μ is the electron mobility, we measure the conductivity of sputtered films annealed at 500 °C and then 800 °C in another attempt to estimate donor density values. Figure 5 shows the dark current density, *J*, as a function of applied potential for samples where the FTO layer is grounded and voltage is applied to a top contact of Au. The 800 °C sample shows rectifying behavior similar to that expected for a diode or junction between a metal and n-type semiconductor. The 500 °C sample shows symmetric photocurrents less than 1.5×10^{-6} A/cm^2 over the range -2.5 V to 2.5 V and less than

0.3×10^{-3} A/cm^2 over the range -25 V to 25 V. This behavior is expected for an insulator and a breakdown field near 0.5×10^6 V/cm for the 600 nm thick α-Fe_2O_3 layer was measured, somewhat lower than the $\approx 10^7$ V/cm breakdown field typically observed for high quality compact oxides with higher energy gaps.[30]

The inset of Fig. 5 shows the specific resistance calculated using

$$\rho = \left(\frac{dJ}{dV}\right)^{-1} \frac{1}{d} \quad (4)$$

where ρ is the resistance in Ω × cm and d is the oxide thickness of 600 nm. Clearly, the sample annealed at 800 °C with higher Sn loading displays a resistance that is between 3 and 6 orders of magnitude lower than that annealed at 500 °C, consistent with doping by group IV elements in α-Fe_2O_3.[33,34] Such a significant reduction in resistance is likely to contribute to the large difference in photocurrent observed between the two samples. The right ordinate of the inset displays the donor density calculated assuming a mobility for hematite of 0.01 cm^2/(V·s).[6] For potentials above 1 V, the effective number density of the Sn atoms asymptotically approaches $N_d \approx 10^{17}$/cm^3 for the sputtered sample annealed at 800 °C. A similar analysis would give a value of $N_d \approx 10^{10}$/cm^3 for the sample annealed only at 500 °C, which is unrealistically low considering typical intrinsic carrier densities and suggests that such an analysis is inappropriate for this insulating material.

Dynamic secondary ion mass spectrometry

In addition to the methods previously discussed, dynamic secondary ion mass spectrometry (SIMS) is employed to quantify Sn doping as a function of distance from the interface between α-Fe_2O_3 and FTO. SIMS measurements on the hydrothermal samples are not readily interpreted

due to the uneven coverage on the FTO surface (Figures S2 and S3 in SI) leading to the motivation for creating sputtered α-Fe_2O_3 films with uniform coverage and thickness which are better suited to SIMS analysis. The mass spectrometer signal in Fig. 6 corresponds to ^{56}Fe and ^{120}Sn averaged over three runs. The increase in Fe signal around 1200 nm corresponds to overlap between ^{56}Fe and two ^{28}Si, demonstrating that the total thickness of α-Fe_2O_3 and FTO layers was approximately 1200 nm, as expected. The FTO layer gave a number density of Sn atoms on the order of $10^{22}/cm^3$ consistent with casserite, SnO_2 (powder diffraction file 41-1445),[35] which has a number density of Sn of $2.8 \times 10^{22}/cm^3$. The average Sn number density over the first 100 nm of material are $(7 \pm 5) \times 10^{17}/cm^3$ and $(7 \pm 1) \times 10^{18}/cm^3$ for the 500 °C and 800 °C sample, respectively, corresponding to mole fractions of cation, Sn/(Sn + Fe), of 0.002 ± 0.001 % and 0.018 ± 0.003 %. It should be emphasized that reported values are approximate and that due to the uneven coverage of the α-Fe2O3 on the FTO substrate, the mole fraction of Sn at the electrolyte interface might contain a small contribution from Sn from the FTO substrate. Nevertheless, the sample annealed at 800 °C displays an increase in Sn concentration by over one order of magnitude. Overall, these results imply that higher temperature annealing promotes diffusion of Sn into the hematite. In addition to driving Sn diffusion, annealing to temperatures 1/2 to 2/3 the host's melting temperature is likely to activate existing dopant impurities.[36] For α-Fe_2O_3, which melts at 1462 °C[37], annealing at 800 °C falls into this range.

Discussion:

Modest improvements in the water oxidation performance of hematite have been achieved by doping combined with nanostructuring.[1,15] Quantifying dopant density using standard semiconductor materials characterization methods requires careful consideration of assumptions and limitations. No single method can be relied upon to provide accurate

quantification. In this work, we set out to determine the donor density in Sn-doped α-Fe_2O_3 samples using a variety of spectroscopic and electrical methods. In all cases, electron microscopy and associated spectroscopies were not sufficiently sensitive to quantify the low Sn concentrations. The Mott-Schottky technique, interpreted using a one dimensional model, consistently gives higher effective N_d than those obtained from SIMS. However, using a model appropriate for a cylindrical geometry yields N_d values in closer agreement with SIMS results. The values of N_d can be reconciled at 10^4 Hz if a surface roughness of ≈13 is included in the linear model. We conclude, however, that N_d cannot be obtained with certainty using capacitance measurements for the current samples because (i) the FTO substrate is both in series and parallel with α-Fe_2O_3layer, (ii) for similar exposed area, the FTO has a capacitance on the same order of magnitude as the sputtered and hydrothermal substrates, (iii) the value of N_d varies by more than two orders of magnitude depending on the chosen model, *viz.* Eq. (1) or (3), and (iv) calculated values of N_d depend on frequency.[7,32,38] These findings suggest that dopant concentrations determined using capacitance results should be reported with caution for metal oxide semiconductors.

The conductivity measurements on sputtered samples annealed at 800 °C yields estimated N_d values that are considerably lower than those obtained from SIMS, suggesting that not all of the Sn present in the samples is actually active. This hypothesis is consistent also with the finding that the Sn concentrations determined by SIMS in sputtered samples annealed at 800 °C *vs.* 500 °C differ by only one order of magnitude, whereas the conductivity differs by at least five orders of magnitude and the photocurrent measured from these two electrodes at 1.23 V differs by at least three orders of magnitude. Considered together, our results indicate that activating the Sn dopant by thermal treatment is crucial for increasing the photocurrent, and hence the

efficiency. Observation of a densification of the α-Fe_2O_3 upon annealing at 800 °C in the STEM-HAADF images could explain one mechanism of activation, because Sn could incorporate into octahedral Fe sites during structural rearrangement and lattice defects could be eliminated. The exact method for incorporation of the Sn is not certain and although our results have been presented considering diffusion of Sn through the solid phase.

Sputtered hematite films doped with Sn offer an easily-prepared, inexpensive material for solar water splitting. Doping with Sn is necessary to achieve photocurrent, but increasing the dopant mole fraction up to 10 % for Sn[1] or 1.5 for Si[39] results in only modest improvements, <2.5 mA/cm^2 at 1.23 V. Processes like rapid thermal annealing, which permit dopant activation or local reorganization of atoms on short time scales, while avoiding long range diffusion of dopants which requires comparatively longer time scales, could prove useful for activating dopants in metal oxide materials used in water splitting.

Conclusion:

Sputtered hematite on FTO coated glass produces photocurrents as high as 1.3 mA/cm^2 at 1.6 V under 100 mW/cm^2 illumination after annealing at 800 °C for 10 min. Annealing at 800 °C results in a marked increase in size of the individual grains, but this change had a minimal effect on activity. Sn incorporation *via* diffusion and activation are found to be critical for producing photocurrent in α-Fe_2O_3. The gradient of Sn is measured as a function of distance from the FTO interface for the first time and the cation mole fraction is found to be approximately 0.02 % Sn at the electrolyte interface, which is considerably lower than previous estimates (10 % Sn) for similarly prepared samples.[1] It is suggested that only a fraction of this Sn contributes to increased activity. The measured change in photocurrent is most likely a result of the decreased specific

resistance that occurs upon annealing to 800 °C. Further steps towards the rational design of photoanodes from inexpensive and earth abundant α-Fe_2O_3 for storing solar energy as hydrogen should be possible with consideration for distribution and activation of dopants by thermal processes.

Acknowledgement:

We acknowledge the support of Fred Sharifi with reactive sputtering, Henri Lezec for advice on FIB milling, Nikolai Zhitenev for discussions on measurements, Glenn Holland for machining the electrochemical cell as well as Alan Band and Dave Rutter for assistance with electronics. Erich Walter acknowledges support from the National Institute of Standards and Technology American Recovery and Reinvestment Act Measurement Science and Engineering Fellowship Program, Award 70NANB10H026, through the University of Maryland.

Supporting Information:

Additional information regarding synthesis, optical characterization, X-ray characterization, electron microscopy, SIMS and the solution of the Poisson equation in cylindrical coordinates is included. This material is available free of charge via the Internet at http://pubs.acs.org.

References and Notes:

(1) Ling, Y.; Wang, G.; Wheeler, D.A., Zhang, J.Z.; Li, Y. *Nano Lett.* **2011**, *11*, 2119-2125.
(2) Morrish, R.; Rahman, M.; MacElroy, J.M.D.; Woldon, C.A. *ChemSusChem* **2011**, *4*, 474-479.
(3) Grätzel, M. *Nature* **2001**, *414*, 338-344.
(4) Sivula, K.; Le Formal, F.; Grätzel, M. *ChemSusChem* **2011**, *4*, 432-449.
(5) Pourbaix, M. *Atlas of electrochemical equilibria in aqueous solutions*. National Association of Corrosion Engineers: Houston, 1974; pp 307-321.
(6) Morin, F.J. *Phys. Rev.* **1954**, *93*, 1195-1199.
(7) Launay, J.C.; Horowitz, G. *J. Cryst. Growth* **1982**, *57*, 118-124.
(8) Kennedy, J.H.; Frese, K.W. *J. Electrochem. Soc.* **1978**, *125*, 723-726.
(9) Kennedy, J.H.; Frese, K.W. *J. Electrochem. Soc.* **1978**, *125*, 709-714.
(10) Lindgren, T.; Vayssieres, L.; Wang, H.; Lindquist, S. In *Chemical physics of nanostructured semiconductors*; Kokorin, A.I., Bahnemann, D.W., Eds.; VSP: Boston, 2003; pp 83-110.
(11) Sivula, K.; Zboril, R.; Le Formal, F.; Robert, R.; Weidenkaff, A.; Tucek, J.; Frydrych, J.; Grätzel, M. *J. Am. Chem. Soc.* **2010**, *132*, 7436-7444.
(12) Glasscock, J.A.; Barnes, P.R.F.; Plumb, I.C.; Savvides, N. *J. Phys. Chem. C* **2007**, *111*, 16477-16488.
(13) Cesar, I.; Sivula, K.; Kay, A.; Zboril, R.; Grätzel, M. *J. Phys. Chem. C* **2009**, *113*, 772-782.
(14) Spray, R.L.; McDonald, K.J; Choi, K.S. *J. Phys. Chem. C.* **2011**, *115*, 3497-3506.
(15) Tilley, D.S.; Cornuz, M.; Sivula, K.; Grätzel, M. *Angew. Chem. Int. Ed.* **2010**, *49*, 6405-6408.
(16) Wijayantha, K.G.; Saremi-Yarahmadi, S.; Peter, L.M. *Phys. Chem. Chem. Phys.* **2011**, *13*, 5264-5270.
(17) Peter, L.M.; Wijayantha, K.G.; Tahir, A. A. *Faraday Discuss.* **2012**, *155*, 309-322.
(18) Vayssieres, L.; Beermann, N.; Lindquist, S. E.; Hagfeldt, A. *Chem. Mater.* **2001**, 13, 233-235.
(19) Bard, A.J.; Faulkner, L.R. *Electrochemical methods: Fundamentals and applications*. 2nd Ed. Wiley: New York, 2001; inside cover.
(20) Ritchie, N.W.M. *Microsc. Microanal.* **2009**, *15*, 454-468.
(21) Krivanek, O.L.; Mory, C.; Tence, M.; Colliex, C. *Microsc. Microanal. Microstruct.* **1991**, *2*, 257-267.
(22) Isaacson, M.; Johnson, D. *Ultramicroscopy* **1975**, *1*, 33-52.
(23) Colliex, C.; Manoubi, T.; Ortiz, C. *Phys. Rev. B* **1991**, *44*, 11402-11411.
(24) van Aken, P. A.; Liebscher, B. *Phys. Chem. Miner.* **2002**, *29*, 188-200.
(25) Egerton, R. *Electron Energy-loss Spectroscopy in the Electron Microscope*, 3rd ed. Springer: New York, 2011.
(26) Orazem, M.E.; Tribollet, B. *Electrochemical Impedance Spectroscopy*. Wiley: New York, 2001; pp 225-230.
(27) Wilhelm, S.M.; Yun, K.S.; Ballenger, L.W.; Hackerman, N. *J. Electrochem. Soc.* **1979**, *126*, 419-424.
(28) Turner, J.E.; Hendewerk, M,; Parmeter, J.; Neiman, D.; Somorjai, G.A. *J. Electrochem. Soc.* **1984**, *131*, 1777-1783.
(29) Cardon, F.; Gomes, W.P. *J. Phys. D: Appl. Phys.* **1978**, *11*, L63-L67.
(30) Sze, S.M. *Physics of Semiconductor Devices*, 2nd ed. Wiley: New York, 1981; pp 406.

(31) Mora-Seró, I.; Fabregat-Santiago, F.; Denier, B.; Bisquert, J.; Tena-Zaera, R.; Elias, J.; Lévy-Clément, C. *App. Phys. Lett.* **2011**, *89*, 203117.
(32) Benko, F.A.; Longo, J.; Koffyberg, F.P. *J. Electrochem. Soc.* **1985**, *132*, 609-613.
(33) Sanchez, H.L.; Steinfink, H.; White, H.S. *J. Solid State Chem.* **1982**, *41*, 90-96.
(34) Liao, P.; Toroker, M.C.; Carter, E.A. *Nano Lett*. **2011**, *11*, 1775-1781.
(35) PDF, Powder Diffraction File, produced by International Centre for Diffraction Data, 12 Campus Blvd., Newtown Square, PA. 19073-3273, USA.
(36) Pearton, S.J. *Processing of wide band gap semiconductors*. William Andrew Publishing: New York, 2000. pp 312.
(37) Barin, I.; Knacke, O. *Thermodynamical properties of inorganic substances.* Springer-Verlag: Berlin, 1973.
(38) Yun, K.S.; Wilhelm, S.M.; Kapusta, S.; Hackerman, N. *J. Electrochem. Soc.* **1980**, *127*, 85-90.
(39) Kay, A.; Cesar, I.; Grätzel, M. *J. Am. Chem. Soc.* **2006**, *128*, 15714-15721.

Table 1. Flat band potential, V_{FB} (V), and Sn donor density, $N_d \times 10^{-19}$ (/cm^3) for sputtered and hydrothermal samples of α-Fe_2O_3 annealed at 500 °C for 2 h (500 °C) or 500 °C for 2 h followed by 800 °C for 10 min (800 °C). All values were derived from Fig. 4 using either linear or radial fits.

		Sputtered			Nanowires	
Hz	Fitted Parameters	800°C		500°C	800°C	500°C
		Radial Fit	Linear Fit	Linear Fit	Linear Fit	Linear Fit
10^4	V_{FB}	0.23±0.02	0.50±0.10	-0.19 ±0.07	0.52±0.03	0.25±0.05
	N_d	0.020±0.001	3.4±0.3	0.8±0.1	3.1±0.1	2.5±0.2
10^3	V_{FB}	0.29±0.03	0.50±0.09	0.15 ±0.10	0.44±0.04	0.40±0.07
	N_d	0.025±0.002	9.3±0.5	1.1±0.1	11.1±0.1	3.8±0.2
10^2	V_{FB}	0.38±0.05	0.56±0.09	0.38±0.09	0.51±0.03	0.55±0.05
	N_d	0.026±0.004	12.4±0.7	1.1±0.1	14.5±0.1	3.9±0.1

Figure 1. (a) Current density (J) versus potential plots for α-Fe_2O_3 sputtered (red) and hydrothermal samples (black) after annealing at 500 °C for 2 h followed by 800 °C for 10 min. (b) Incident photon to current efficiency (IPCE) *vs.* wavelength (λ) at V_{RHE} = 1.23 V for α-Fe_2O_3 sputtered and hydrothermal samples annealed at 500 °C for 2 h followed by 800 °C for 10 min. Insets show SEM cross-sections of the sputtered (thickness 600 nm ± 30 nm) and hydrothermal (thickness 300 nm ± 30 nm) samples after annealing. Shading indicates a single standard deviation calculated from at least three experiments.

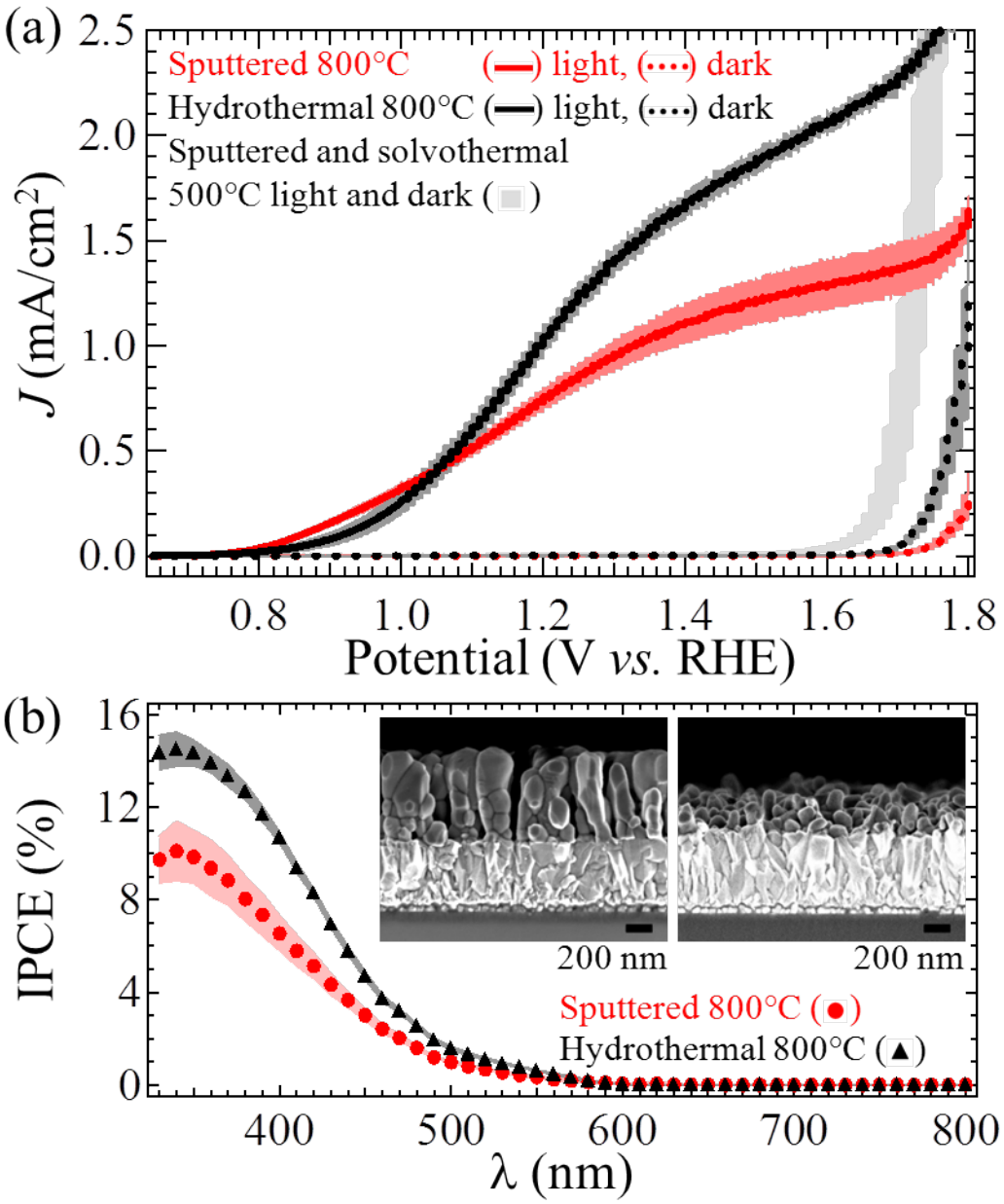

Figure 2. SEM images of cross-sectioned α-Fe_2O_3 sputtered films (a) annealed at 500 °C for 2 h and (b) further annealed at 800 °C for 10 min. Four distinct layers are present: 2000 nm Pt, 600 nm of sputtered α-Fe_2O_3, 600 nm of FTO and float glass. The scale bar is 1 µm. (c) EDS linescans for Fe $K_{\alpha 1}$ and Sn $L_{\alpha 1}$ corresponding to the black lines in panels (a) and (b) for samples annealed at 500 °C (black) and 800 °C (red). The apparent interfacial width is due most likely to the x-ray generation point spread function rather than diffusion.

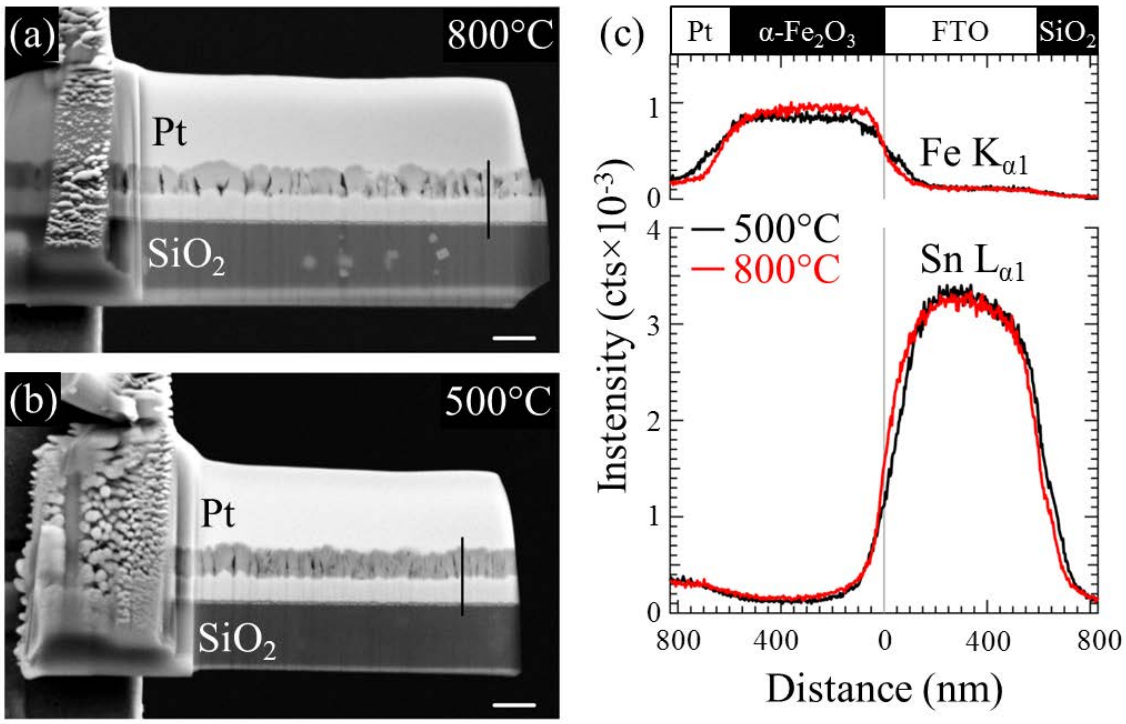

Figure 3. STEM-HAADF images and EELS results for 100 nm thick cross-sections of sputtered hematite films obtained from the specimen in Fig. 2. In (a) and (b), the FTO substrate is visible as a light underlayer, the Pt as the light overlayer. (a) 500 °C annealed sample. (b) 500 °C then 800 °C annealed sample. (c) O K-edge and Sn $M_{4,5}$-edge for the α-Fe_2O_3 layers for 500 °C annealed sample (black), 800 °C annealed sample (red), and FTO substrate (blue). Broad delayed Sn $M_{4,5}$-edges at 485 eV and 493 eV are indicated by down arrows in (c) for the FTO sample. (d) Fe $L_{3,2}$-edges for 500 °C annealed sample (black), 800 °C annealed sample (red), and FTO substrate (blue).

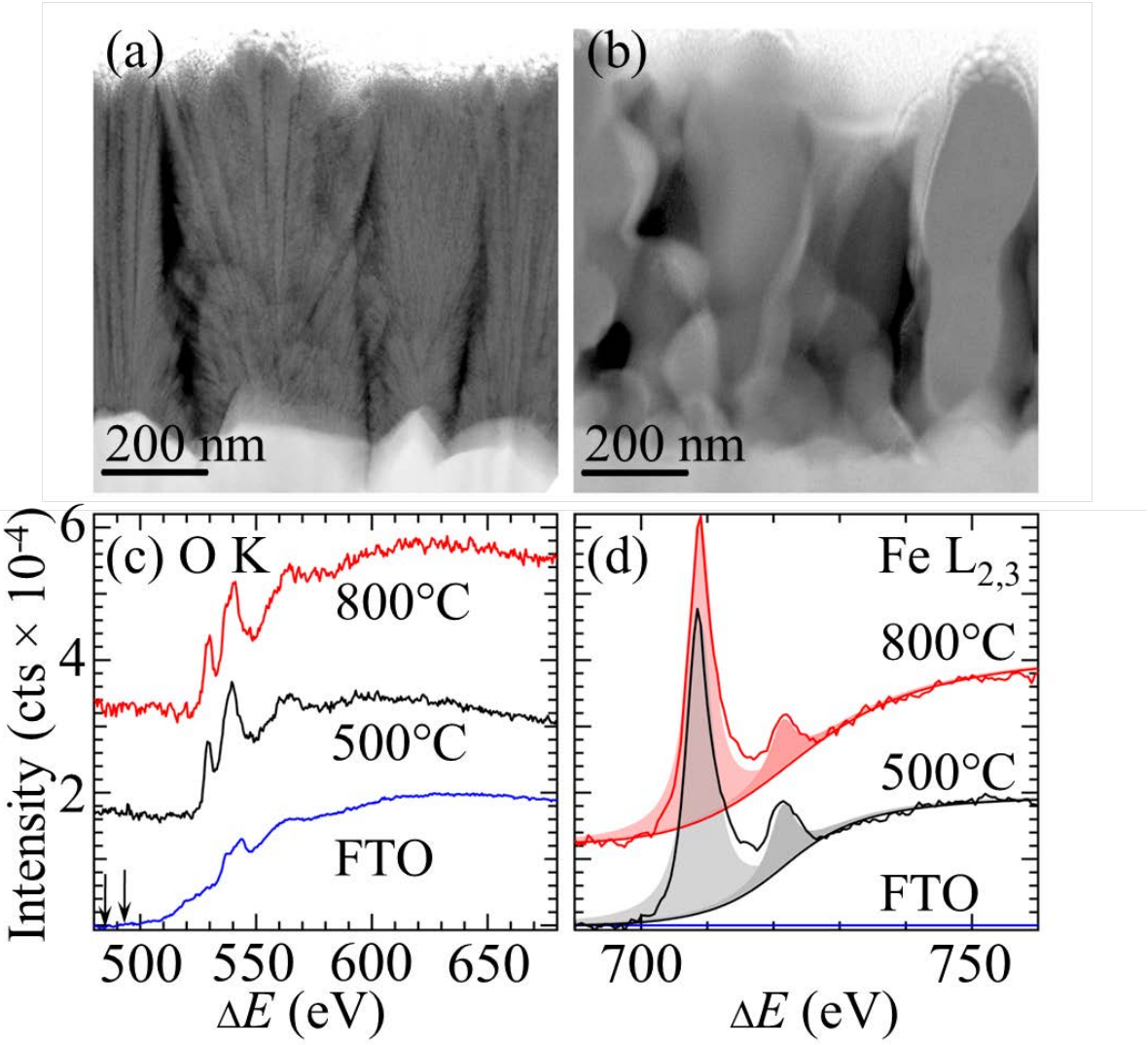

Figure 4. Mott-Schottky plots of the square of the inverse capacitance *vs*. potential for sputtered and hydrothermal α-Fe_2O_3 samples at 10^2 Hz (blue), 10^3 Hz (black) and 10^4 Hz (red). Samples had been annealed at 500 °C for 2 h (b, d), followed by 800 °C for 10 min (a, c). Linear fits using Eq.(1) between 0.6 V and 1.2 V and radial fits using Eq.(3) corrected for geometrical area (see SI for details) between 0.3 V and 0.9 V were used to determine the flat band potential, V_{FB}, and donor density, N_d, and are shown in (e) and (f), respectively. Above approximately 1.6 V, water splitting commenced causing a decrease in C^{-2}. Shading, in (a) through (d), indicates a single standard deviation calculated from at least three experiments.

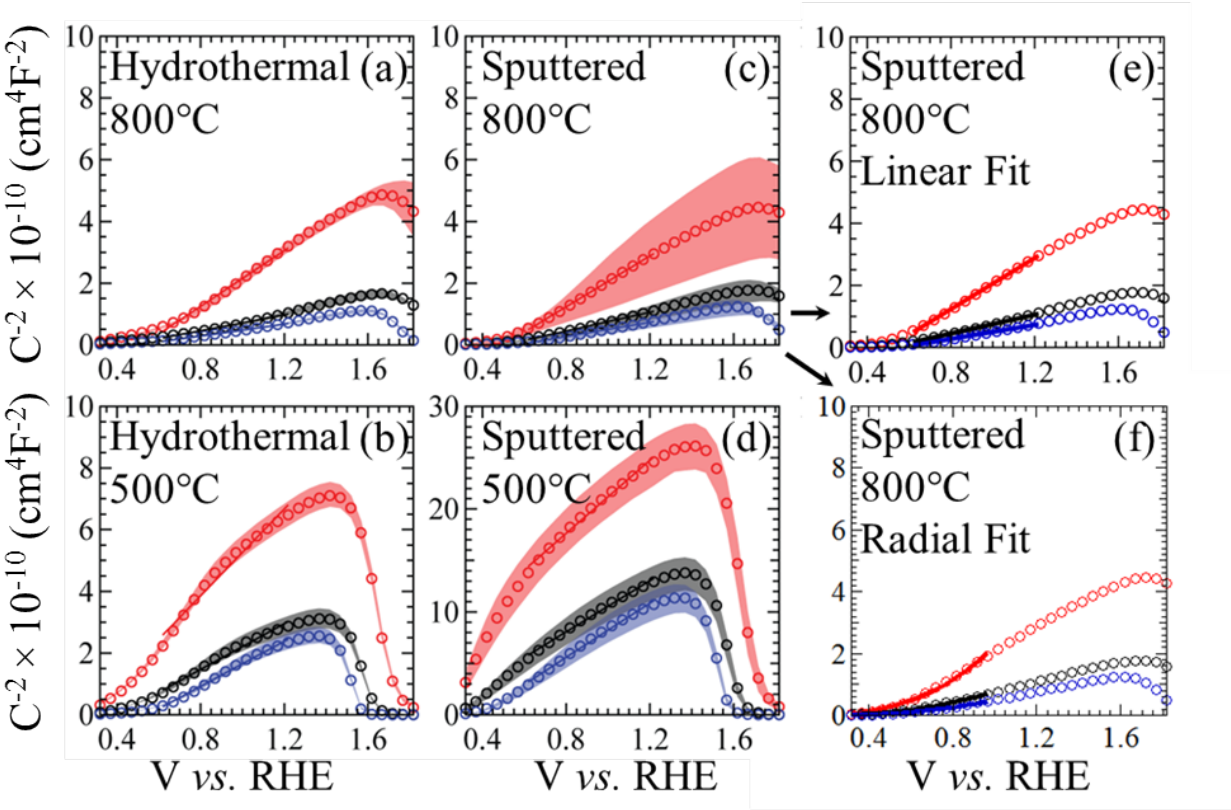

Figure 5. *J-V* curves for sputtered α-Fe_2O_3 on FTO annealed at 500 °C for 2 h (black), followed by 800 °C for 10 min (red). The inset shows the specific electrical resistance (left axis) and resulting donor density, N_d (right axis), as a function of potential. Shading indicates a single standard deviation calculated from at least ten experiments.

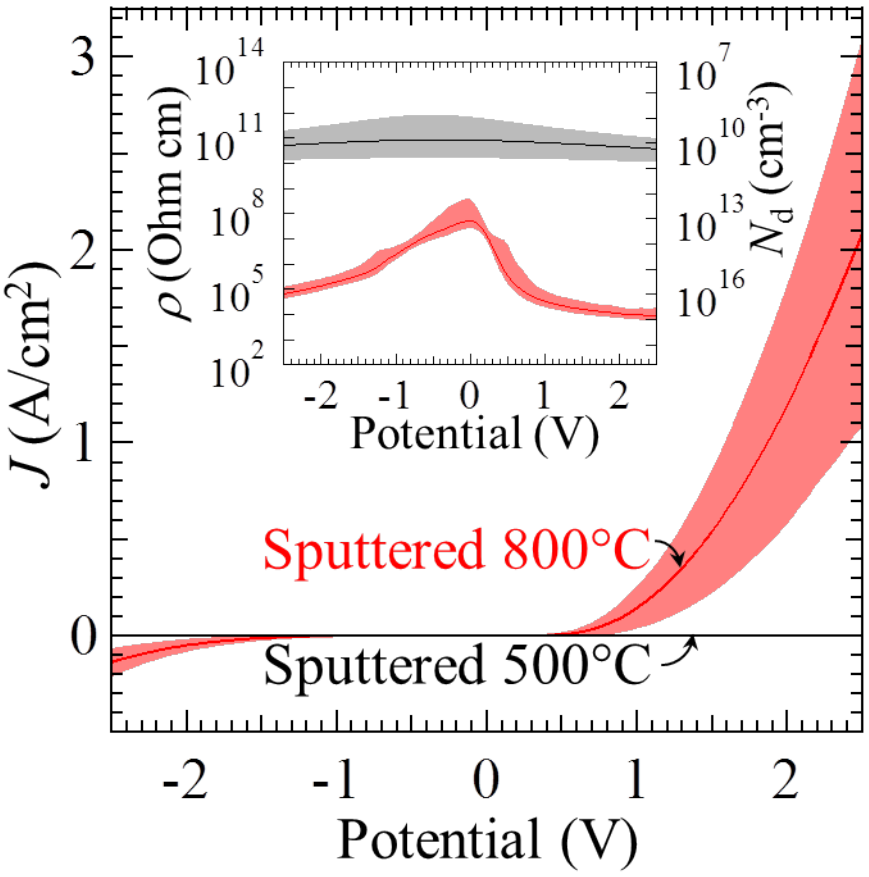

Figure 6. Dynamic SIMS of ^{120}Sn and ^{56}Fe from sputtered films of α-Fe_2O_3 on FTO coated soda lime float glass annealed at 500 °C for 2 h (black), followed by 800 °C for 10 min (red) assuming a linear sputtering rate (see SI). The interface between α-Fe_2O_3 and FTO is marked by an arrow; the interface between FTO and float glass also is indicated. Quantification is approximate. Shading indicates a single standard deviation calculated from at least three experiments.

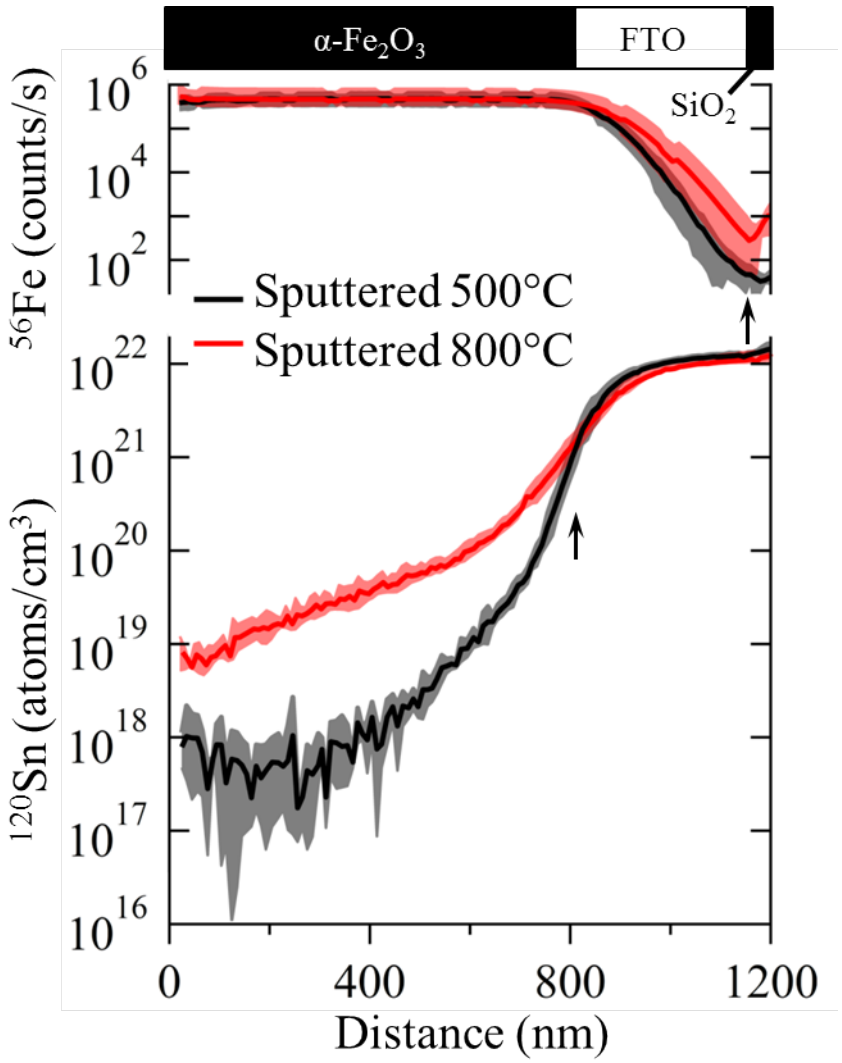

Figure for Table of Contents:

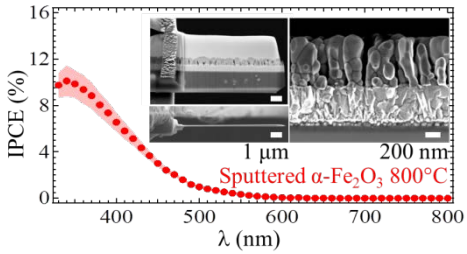

Supporting Information

The Effect of Tin Doping on α-Fe_2O_3 Photoanodes for Water Splitting

Christopher D. Bohn[1†], Amit K. Agrawal[1,2], Erich C. Walter[1,3], Mark D. Vaudin[4], Andrew A. Herzing[5], Paul M. Haney[1], A. Alec Talin[1], Veronika A. Szalai[1†]

[1] Center for Nanoscale Science and Technology, National Institute of Standards and Technology, Gaithersburg, Maryland, 20899, USA.

[2] Dept. of Electrical Engineering and Computer Science, Syracuse University, Syracuse, NY, 13244, USA.

[3] Institute for Research in Electronics and Applied Physics (IREAP), University of Maryland, College Park, MD 20742, USA.

[4] Ceramics Division, National Institute of Standards and Technology, Gaithersburg, MD, 20899, USA.

[5] Surface and Microanalysis Science Division, National Institute of Standards and Technology, Gaithersburg, MD 20899, USA.

[†]Corresponding authors. Phone: 301-975-3792 (VAS), 301-975-4236 (CDB), Fax: 301-975-2303, Email: veronika.szalai@nist.gov, christopher.bohn@nist.gov

Synthesis details

For sputtered samples, depositions required a power of 200 W at 0.4 A to give 0.3 nm/s of α-Fe_2O_3 at room temperature with gas flowrates of O_2 (12 mL/min) and Ar (50 mL/min). The α-Fe_2O_3 film thickness was measured by profilometry and confirmed by SEM cross-section.

For hydrothermal samples, a solution of 0.15 mol/L iron chloride hexahydrate ($FeCl_3 \cdot 6H_2O$ mass fraction >99 %) and 1 mol/L sodium nitrate ($NaNO_3$ mass fraction >99 %) was brought to pH 1.5 by the addition of 1 mol/L hydrochloric acid. One FTO slide was placed conducting side up in a sealed glass container with 20 mL of solution and heated for 4 h at 95 °C,

and then immediately rinsed with deionized water. After preheating a muffle furnace, slides were placed in an air atmosphere for 2 h at 500 °C and promptly removed. The thickness of the resulting hydrothermal α-Fe_2O_3 was 300 nm ± 30 nm as determined by SEM. After permitting samples to cool to room temperature, further annealing was performed in some cases by preheating the furnace to 800 °C, inserting samples followed by rapid removal after 10 min.

A control sample was prepared by sputtering α-Fe_2O_3 with a thickness of 600 nm on 200 nm of Au with an adhesion layer of 20 nm Cr on float glass. This sample was annealed under the same conditions as the sputtered and hydrothermal samples but demonstrated no photocurrent, as shown in Fig. S1. Because annealing at 800 °C approached the melting temperature of the Au (1164 °C), a multimeter was used to measure the resistance of the Au layer before and after annealing to confirm that it remained conductive. Poisoning of the surface by evaporated Au can be ruled out because all slides were annealed together.

Two methods were attempted to determine the surface area of the samples. First monolayers of Orange II dye were deposited.[S1,S2] This method gave inconclusive results. The second method, krypton gas adsorption with diced samples, also returned inconclusive results. On the basis of the adsorption instrument's sensitivity, however, we estimate the roughness factor, defined as the real area divided by the geometric area, to be on the order of 20 or less for both the sputtered and hydrothermal samples that were annealed at 800 °C. In all calculations presented in the text, the geometric area was used for normalization.

Optical characterization

Figure S2 shows optical images of the sputtered and hydrothermal α-Fe_2O_3 samples at room temperature, after annealing at 500 °C for 2 h, and after annealing at 800 °C for a further 10 min.

The yellow FeOOH in the room temperature hydrothermal sample contrasts with the red α-Fe_2O_3 of the annealed samples. The samples are less transparent and become deeper red in color after heat treatment. Illumination from the back side demonstrates the non-uniform coverage of the hydrothermal sample.

An ultraviolet-visible spectrophotometer with a photodiode array equipped with tungsten and deuterium lamps was used to measure absorbance from 190 nm to 1100 nm in 1 nm increments. Figure S3 shows absorbance as a function of wavelength for the FTO substrate, hydrothermal and sputtered samples at room temperature, after heating at 500 °C for 2 h, and after further heating at 800 °C for 10 min. The shading indicates the standard deviation of 3 experiments. In all cases, the background absorbance at wavelengths larger than 600 nm increased with heating, which could be ascribed to roughening of the surface, observable by eye, causing increased scattering as well as to the deterioration of the FTO substrate. Considering that the samples annealed at 800 °C have a bandgap that is at most 0.2 eV below the 2.0 eV calculated for samples annealed at 500 °C suggests a difference in available photons for water splitting of at most 6 % between the samples. By contrast, the difference in photocurrent observed at 1.23 V *vs.* RHE is 3 orders of magnitude demonstrating that absorption alone is *not* sufficient to explain the change in photocurrent.

Non-uniform coverage is apparent in the hydrothermal samples as discontinuous absorbance: two strong absorbance lines corresponding to FTO and α-Fe_2O_3 are apparent and are indicated by the two down arrows in S3. Determination of the exact bandgap is difficult owing to the fitting procedure required in a Tauc analysis;[S3] nevertheless, the bandgap for the sputtered and hydrothermal samples at 800 °C can be estimated from the onset of absorbance to between 2.0 eV and 2.2 eV. A shift in absorbance towards longer wavelengths is observable for

both the sputtered and hydrothermal samples upon heat treatment suggesting that the bandgap decreases after heating. The incorporation of Sn dopants is the most likely cause of this decrease in bandgap.

X-ray characterization

X-ray diffraction was performed in air at room temperature with a copper source (Cu $K_{\alpha 1}$, λ = 0.15406 nm) at 40 kV and 30 mA. A step of 0.03° and dwell time of 4 s was used with 0.68° and 0.15° divergence and receiving slits, respectively. X-ray diffraction spectra for the synthesized samples annealed at different temperatures as well as for the FTO substrate are shown in Fig. S4. The presence of α-Fe_2O_3 (PDF 33-0664)[S4] is noticeable in the sputtered samples by peaks at 2θ of 35.61° and 63.99°, as indicated by the vertical lines in Fig. S4. The presence of these peaks and the absence of a maximum intensity peak at 24.14° suggest preferential orientation of the c-axis parallel to the substrate. The absence of peaks in the sputtered sample at 30.09° and 56.94°, 41.93°, and 44.67° was used to rule out the formation of Fe_3O_4 (PDF 19-0629), FeO (PDF 6-0615) and Fe (PDF 6-0696), respectively, during sputtering. Smaller peaks corresponding to α-Fe_2O_3 were observed in the hydrothermal samples compared to the sputtered samples after annealing, which could be explained by the smaller thickness and therefore smaller quantity of α-Fe_2O_3 material. For the hydrothermal sample at room temperature, the primary goethite (PDF 29-0713) peak at 21.22° is absent; however, a peak at 35.09° was observed, which may be attributed to akaganeite (PDF 42-1315).

Electron Microscopy Characterization

A focused-ion beam (FIB) instrument with a gallium source and primary beam voltage of 30 kV was used to prepare the 100 nm ± 20 nm thick α-Fe_2O_3 cross-sections; platinum was used as an overlayer and for attachment to the copper grids.

For energy dispersive X-ray spectroscopy (EDS), a primary beam of 10 kV and a 60 µm aperture were used. Calibration was performed with a silicon wafer (Si, K_α of 1.740 keV) and copper tape (Cu, K_α of 8.041 keV). A total of 2×10^7 counts were collected for each sample over 5 h. Sample drift was automatically corrected every 20 s and the maximum drift recorded was <35 nm. Simulations of X-ray generation in α-Fe_2O_3 were performed using NIST's Monte Carlo code DTSA-II (freeware).[S5] For α-Fe_2O_3 (PDF 33-0664) with density 5.26 g/cm^3, a primary beam voltage of 10 kV, the diameter of the X-ray generation volume with the beam perpendicular to the bulk material was determined to be ≈ 0.5 µm.

For scanning transmission electron microscopy (STEM) imaging, a primary beam acceleration of 300 kV was used with a post-column imaging energy-filter operating in spectroscopy mode for EELS acquisition. A 2.5 mm entrance aperture, 16 mrad illumination semiangle, 16 mrad collection semiangle, and energy dispersion of 0.5 eV/channel were used. Typically, 20 spectra were collected for approximately 0.7 s each over an area of 30 nm × 30 nm or at a single point. The spectra for the 500 °C sample were collected 200 nm from the FTO interface, while those for the 800 °C sample were collected at a distance of 70 nm but showed no noticeable variation with increasing distance from the interface.

For the EELS spectra, a power law background of the form:

$$f(\Delta E) = a\Delta E^{-b}, \quad \text{(S.1)}$$

where *a* and *b* are fitting parameters and ΔE is the energy loss, was subtracted using the windows 400 eV to 470 eV for Fig. 3(c) and 650 eV to 680 eV for Fig. 3(d). The intensity, *I*, of the Fe L_3 and L_2-edges was further calculated as follows. A background function of the form of Eq.(S.2) was subtracted:

$$f(\Delta E) = \frac{h_1}{\pi}\left\{\tan^{-1}\left[\frac{\pi}{w_1}(\Delta E - E_1)\right] + \frac{\pi}{2}\right\} + \frac{h_2}{\pi}\left\{\tan^{-1}\left[\frac{\pi}{w_2}(\Delta E - E_2)\right] + \frac{\pi}{2}\right\}, \quad \text{(S.2)}$$

where h_1,w_1, h_2 and w_2 are fitting parameters and $E_1 = 709$ eV and $E_2 = 721.5$ eV. This background function was fit over the intervals 650 eV to 700 eV and 730 eV to 780 eV and is shown in Fig. 3. Next, a Lorentzian function was fit over 650 eV to 780 eV to determine peak areas:

$$f(\Delta E) = \frac{h_1}{\pi}\left\{\frac{\frac{1}{2}w_1}{(\Delta E - E_1)^2 + \left(\frac{1}{2}w_1\right)^2}\right\} + \frac{h_2}{\pi}\left\{\frac{\frac{1}{2}w_2}{(\Delta E - E_2)^2 + \left(\frac{1}{2}w_2\right)^2}\right\}, \quad \text{(S.3)}$$

where h_1,w_1, h_2 and w_2 are unique fitting parameters and $E_1 = 709$ eV and $E_2 = 721.5$ eV as before. The ratio of $I(L_3)/I(L_2)$ was calculated using h_1/h_2 from Eq.(S.3) and gave 5.0 and 6.0 for the 500 °C and 800 °C sputtered samples, respectively, in agreement with published values of 4.7 to 6.5 for α-Fe_2O_3.[S6,S7]

SIMS characterization

The secondary ion was O_2^+; an accelerating potential of 8 kV and current of 100 nA was used; material was removed from a raster area of 150 µm × 150 µm. Distance was calculated by multiplying the instantaneous time of collection by the final crater depth, 1300 nm in in all cases, and dividing this product by the total acquisition time of approximately 22 min. This calculation assumes a linear sputtering rate, which our experimental data indicate is not entirely correct. For

600 nm thick hematite films, the interface was observed at 800 nm, using the distance calculation described above. To correctly recover the interface between α-Fe_2O_3 and FTO at 600 nm, the sputter rate in the α-Fe_2O_3 should be half that in the FTO. This difference is reasonable given the difference in chemical composition of the layers. The detection limit of the instrument based on a dynamic range of approximately six orders of magnitude was fixed at $10^{16}/cm^3$.

Solution to Poisson Equation

The Poisson equation is given by:

$$\nabla^2 V = \frac{-qN_d}{\epsilon\epsilon_0}. \tag{S.4}$$

Assuming a cylindrical geometry with a nanowire of radius, R, centered at $r = 0$ and a charge density which is uniform between r_0 and R and vanishes in the interior $(r < r_0)$, the potential difference between the interior and exterior of the wire is given by:

$$\left(V - V_{FB} - \frac{kT}{q}\right) + \frac{qN_d}{2\epsilon\epsilon_0}\left[\frac{(R^2 - r^2)}{2} + R^2 ln\left(\frac{r}{R}\right)\right] = 0, \tag{S.5}$$

where $R - r$ is the space charge width, V_{FB} is the flatband potential, T is the temperature, k is Boltzmann's constant, q is the elementary charge, N_d is the dopant density, ϵ is the relative permittivity of the semiconductor, ϵ_0 is permittivity of free space, r is the radius and $V(R) = V_{FB} + kT/q$.[S8] Considering the cylindrical structure of the α-Fe_2O_3 with radii of $R = 100$ nm in Figs. 1-3, most of the charge is contained in the cylinder's walls, $Q = qN_D\pi(R^2 - r^2)L$, over area $A = 2\pi RL$. The capacitance per unit area is then calculated using the expression for Q and Eq. (S.5) for V as:

$$C = \frac{1}{A}\frac{dQ}{dV} = \frac{2\epsilon\epsilon_0 r_0^2}{R(R^2 - r_0^2)}, \tag{S.6}$$

which leads to the Mott-Schottky expression for a cylinder,

$$\frac{1}{C^2} = \left[\frac{R(R^2 - r^2)}{2\epsilon\epsilon_0 r_0^2}\right]^2, \tag{S.7}$$

where r_0 is a function of V. For consistency with experimental results, however, the geometrical area must be used for normalization of the capacitance, and it is assumed that the geometrical area is one tenth the area of the cylinder side walls since for hexagonally closest packing, $\frac{\pi R^2}{0.91} \times \frac{1}{2\pi RL} \approx \frac{1}{10}$. This assumption also justifies ignoring surfaces perpendicular to the side walls in the calculation of capacitance and was used in plotting the curves in Fig. 4(f).

SI References:

(S1) Kay, A.; Cesar, I.; Grätzel, M. *J. Am. Chem. Soc.* **2006**, *128*, 15714-15721.
(S2) Bandara, J. ; Mielczarski, J. A.; Kiwi, J. *Langmuir* **1999**, *15*, 7670-7679.
(S3) Tauc, J.; Grigorovici, R.; Vancu, A. *Phys. Status Soidi* **1966**, *15*, 627-637.
(S4) PDF, Powder Diffraction File, produced by International Centre for Diffraction Data, 12 Campus Blvd., Newtown Square, PA. 19073-3273, USA.
(S5) Ritchie, N.W.M. *Microsc. Microanal.* **2009**, *15*, 454-468.
(S6) Colliex, C.; Manoubi, T.; Ortiz, C. *Phys. Rev. B* **1991**, *44*, 11402-11411.
(S7) van Aken, P. A.; Liebscher, B. *Phys. Chem. Miner.* **2002**, *29*, 188-200.
(S8) Mora-Seró, I.; Fabregat-Santiago, F.; Denier, B.; Bisquert, J.; Tena-Zaera, R.; Elias, J.; Lévy-Clément, C. *App. Phys. Lett.* **2011**, *89*, 203117.

Table S1. Four point probe measurements of sheet resistance of the FTO substrates gave (7.5 ± 0.3) Ω × m^2 / m^2 at room temperature, (6.9 ± 0.1) Ω × m^2 / m^2 after annealing at 500 °C for 2 h, and (11.4 ± 0.3) Ω × m^2 / m^2 after annealing at 800 °C for a further 10 min.

	RT	500°C	800°C
ρ (Ω×m^2/m^2)	7.5±0.3	6.9±0.1	11.4±0.3

Figure S1. Current density (*J*) *vs.* potential for α -Fe_2O_3 sputtered samples with a thickness of 600 nm on FTO, hydrothermal samples with a thickness of 300 nm on FTO and sputtered films with a thickness of 600 nm on 200 nm of Au, 20 nm of Cr and float glass. In all cases, samples were annealed at 500 °C for 2 h followed by 800 °C for 10 min. The electrolyte was 1 mol/L NaOH (pH 13.6); calibrated AM 1.5 light at 100 mW/cm^2 illuminated each sample; the scan rate was 10 mV/s. For the sample with Au as the back contact, no Sn doping with heat treatment is possible and no photocurrent is observed leading to the conclusion that doping is indeed necessary for photocurrent. Shading indicates a single standard deviation calculated from at least three experiments.

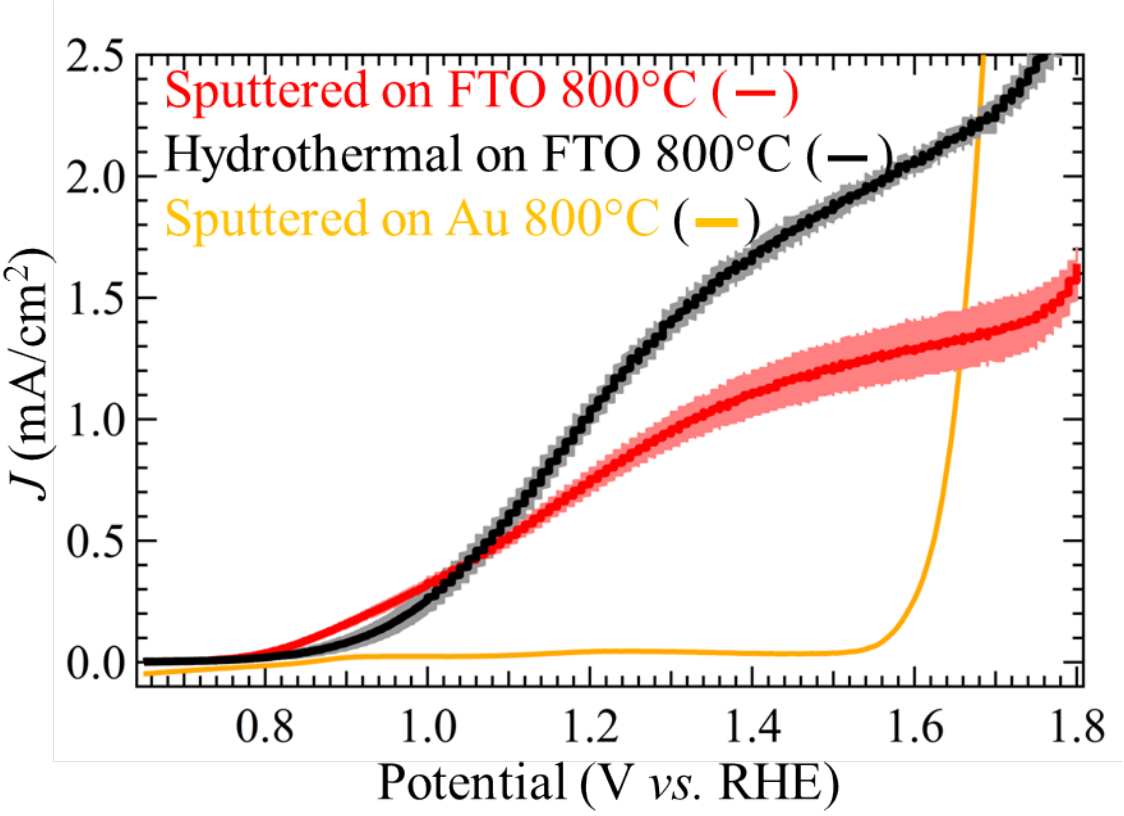

Figure S2. (a) (Top) Optical image of the sputtered α-Fe_2O_3 samples of thickness 600 nm at room temperature, after annealing at 500 °C for 2 h, and after annealing at 800 °C for a further 10 min. (Bottom) Hydrothermal samples of thickness 300 nm at room temperature, after annealing at 500 °C for 2 h, and after annealing at 800 °C for a further 10 min. The yellow FeOOH in the room temperature sample contrasts with the red α-Fe_2O_3 of the annealed samples. (b) Optical image of sputtered and hydrothermal samples after annealing at 800 °C illuminated from the back; the non-uniform coverage of the hydrothermal sample is apparent. Each slide has dimensions of 25 mm × 25 mm. Scanning electron microscope image of the top of sputtered (c) and hydrothermal (d) α-Fe_2O_3 samples annealed at 500 °C for 2 h, followed by 800 °C for 10 min. The larger surface area of the hydrothermal samples in (d) is apparent.

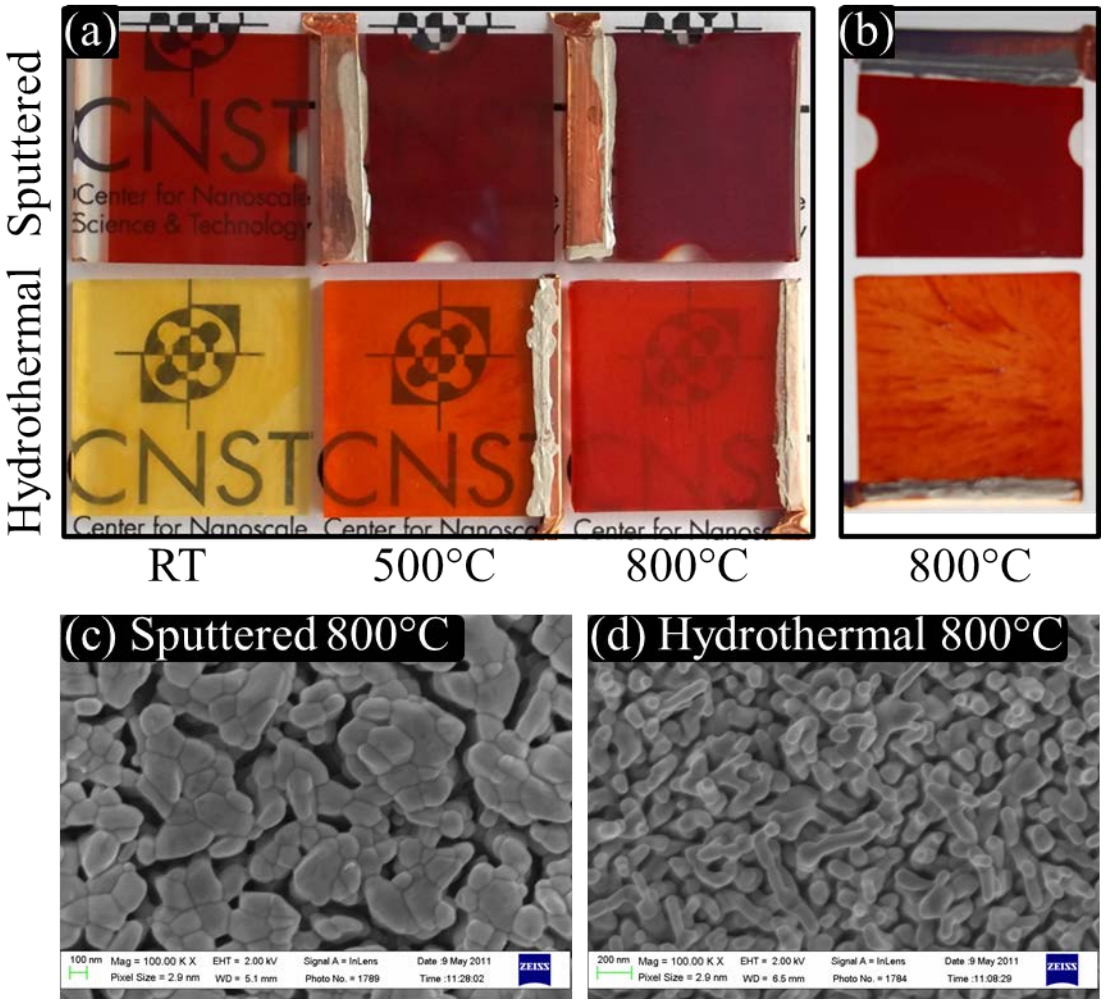

Figure S3. Absorbance versus wavelength (λ) or energy (*E*) of α-Fe_2O_3 sputtered samples of thickness 600 nm on FTO, hydrothermal samples of thickness 300 nm on FTO and blank FTO of thickness 600 nm at room temperature (blue), after annealing at 500 °C for 2 h (black), and after further annealing at 800 °C for 10 min (red). The cut-on absorbance shifts towards higher wavelengths upon heat treatment for the sputtered and hydrothermal samples. Incomplete coverage of the α-Fe_2O_3 in the hydrothermal samples is apparent as two absorbance regions corresponding to α-Fe_2O_3 and FTO are distinguishable, indicated by down arrows. Shading indicates a single standard deviation calculated from at least three experiments.

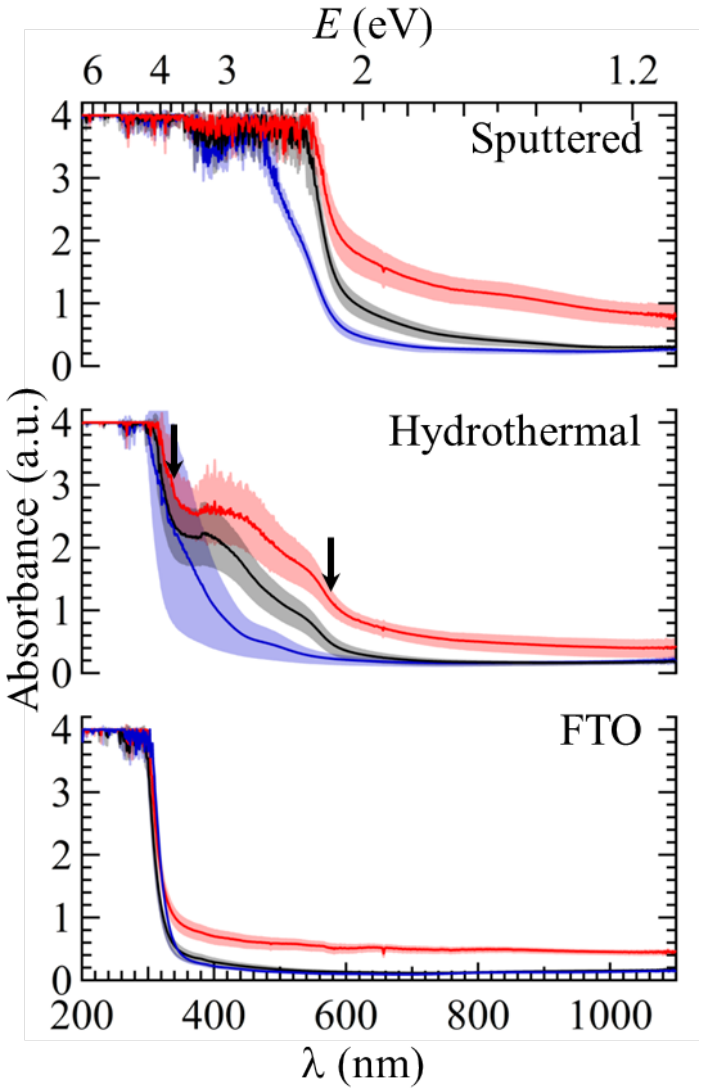

Figure S4. X-ray diffraction patterns in order from bottom to top of eight samples: amorphous soda lime float glass; amorphous soda lime float glass coated with 600 nm FTO; as deposited hydrothermal samples on FTO; hydrothermal samples on FTO heated to 500 °C for 2 h; hydrothermal samples on FTO heated to 500 °C for 2 h followed by 800 °C for 10 min; sputtered α -Fe_2O_3 on FTO; sputtered α -Fe_2O_3 on FTO heated to 500 °C for 2 h; sputtered α -Fe_2O_3 on FTO heated to 500 °C for 2 h followed by 800 °C for 10 min. The thicknesses of the sputtered and hydrothermal samples are 600 nm and 300 nm, respectively.

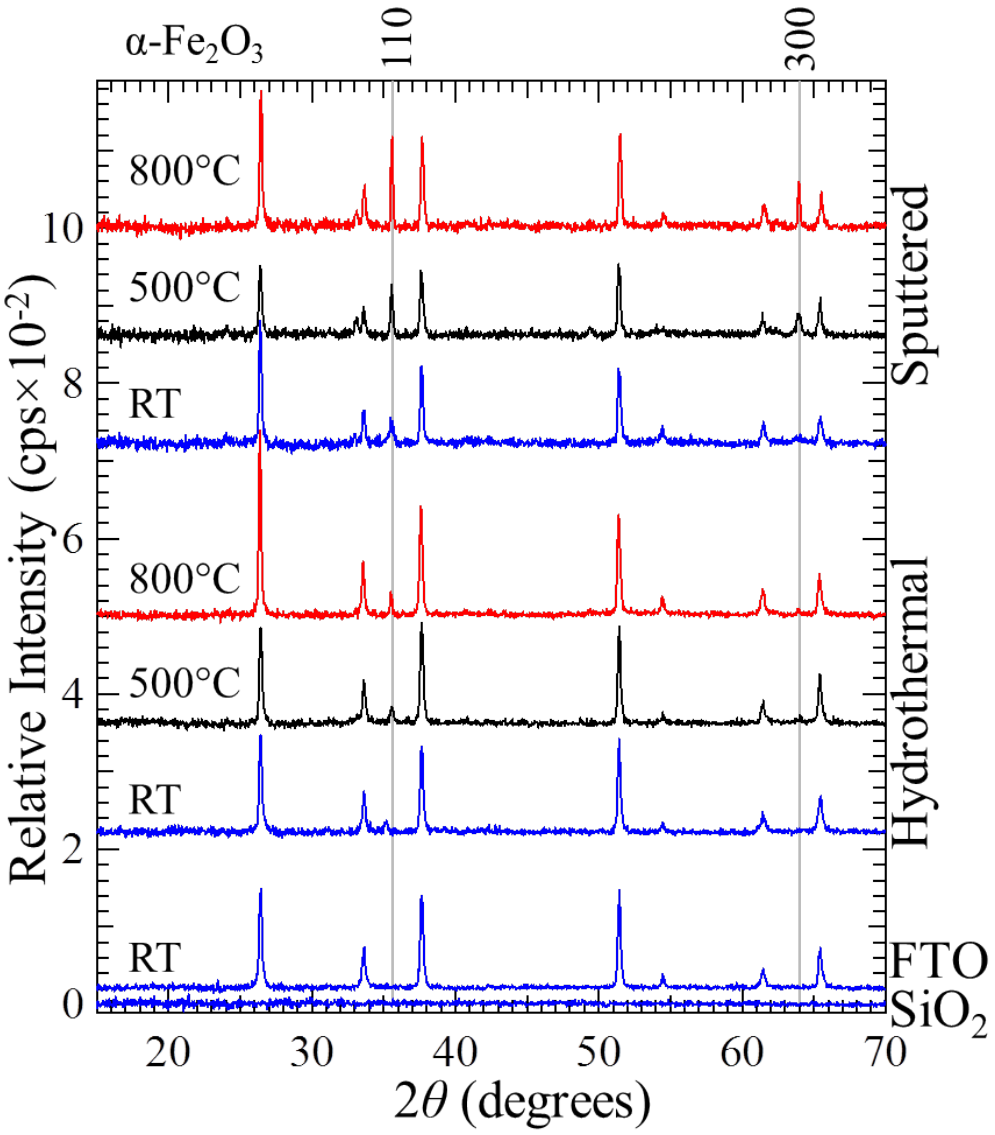

Figure S5. Mott-Schottky plots of the square of the inverse capacitance *vs*. potential for the blank FTO substrate at three different frequencies: 10^2 Hz (blue), 10^3 Hz (black) and 10^4 Hz (red). The electrolyte was 1 mol/L NaOH (pH 13.6); experiments were conducted in the dark; the samples had been annealed at 500 °C for 2 h (a), followed by 800 °C for 10 min (b). Shading indicates a single standard deviation calculated from at least three experiments.